AGU PUBLICATIONS

JGR

Journal of Geophysical Research: Oceans

RESEARCH ARTICLE

10.1002/2017JC013026

Katabatic Wind-Driven Exchange in Fjords

Michael A. Spall[1], Rebecca H. Jackson[2], and Fiammetta Straneo[1]

[1]Woods Hole Oceanographic Institution, Woods Hole, MA, USA, [2]College of Earth, Ocean, and Atmospheric Sciences, Oregon State University, Corvalis, OR, USA

Key Points:
- Katabatic winds can force significant exchange between the fjords and shelf
- Friction limits exchange for narrow fjords
- Exchange in wide fjords is well predicted by two-layer, nonrotating theory

Correspondence to:
M. A. Spall,
mspall@whoi.edu

Citation:
Spall, M. A., Jackson, R. H., & Straneo, F. (2017). Katabatic wind-driven exchange in fjords. *Journal of Geophysical Research: Oceans*, *122*, 8246–8262. https://doi.org/10.1002/2017JC013026

Received 26 APR 2017
Accepted 12 SEP 2017
Accepted article online 27 SEP 2017
Published online 28 OCT 2017

Abstract The general issue of katabatic wind-driven exchange in fjords is considered using an idealized numerical model, theory, and observations. Two regimes are identified. For fjords narrower than a viscous boundary layer width, the exchange is limited by a balance between wind and friction in lateral boundary layers. For the nonlinear viscous parameterization used here, this boundary layer thickness depends on the properties of the fjord, such as stratification and length, as well as on the wind stress and numerical parameters such as grid spacing and an empirical constant. For wider fjords typical of east Greenland, the balance is primarily between wind, the along-fjord pressure gradient, and acceleration, in general agreement with previous two-layer nonrotating theories. It is expected that $O(10\%)$ of the surface layer will be flushed out of the fjord by a single wind event. Application of the idealized model to a typical katabatic wind event produces outflowing velocities that are in general agreement with observations in Sermilik Fjord, a large glacial fjord in southeast Greenland. The presence of a sill has only a minor influence on the exchange until the sill penetrates over most of the lower layer thickness, in which cases the exchange is reduced. It is concluded that the multiple katabatic wind events per winter that are experienced by the fjords along east Greenland represent an important mechanism of exchange between the fjord and shelf, with implications for the renewal of warm, salty waters at depth and for the export of glacial freshwater in the upper layer.

Plain Language Summary Fjords represent an important connection between tidewater glaciers and the shelf ocean. Relatively warm waters from the ocean can melt the glaciers, leading to a loss of glacier mass and an introduction of fresh water to the ocean. We focus here on the influence of katabatic winds, events characterized by strong winds directed down the glacier towards the open ocean, on the exchange of water between the fjord and shelf. Theoretical considerations, computer models, and direct ocean observations in Sermilik Fjord along east Greenland support the conclusion that individual katabatic wind events can result in an exchange of approximately 10% of the fjord water mass. The multiple katabatic events that occur each year thus represent an important mechanism of exchange between the fjords of Greenland and the adjacent shelf.

1. Introduction

1.1. Importance of Fjords

Fjords are garnering increased attention as sites of ocean-glacier interactions. In Greenland, West Antarctica, Alaska, and elsewhere, fjords form conduits between tidewater glaciers and the shelf ocean. In these fjords, the ocean is a source of heat to drive submarine melting of glaciers, icebergs, and sea ice, while the glacier is a source of freshwater to the ocean.

The exchanges of heat and freshwater in fjords are important for both directions of ocean-glacier interaction. First, accelerated mass loss from the Greenland Ice Sheet has been linked to ocean warming (Holland et al., 2008; Motyka et al., 2011; Shepherd et al., 2012; Straneo & Heimbach, 2013), with submarine melting as the presumed connection. Submarine melting should vary with the near-ice ocean temperature (Hellmer & Olbers, 1989), and growing evidence suggests that ocean temperature is closely linked to the net frontal ablation of glaciers (Luckman et al., 2015). However, the drivers of ocean heat transport and warm water renewal that, in part, control submarine melting are poorly understood in glacial fjords (Straneo & Cenedese, 2015). Second, as ice mass loss increases, glaciers are a growing source of freshwater to fjords and,

eventually, the large-scale ocean (Bamber et al., 2012; Gillard et al., 2016). The manner in which this freshwater is mixed and exported from fjords will dictate the freshwater's impact on coastal currents, larger scale circulation, and deep convection. Thus, exchanges of heat and freshwater in fjords are central to the interaction of the ocean and cryosphere.

A variety of mechanisms can modulate these exchanges by driving fjord circulation and fjord/shelf exchange. Buoyancy-driven flows have been the focus of many recent studies. In glacial fjords, surface runoff that discharges at depth (subglacial discharge, hereafter) and submarine melting drive upwelling convective plumes at the ocean-glacier interface (Jenkins, 2011; Mankoff et al., 2016; Sciascia et al., 2013; Xu et al., 2012) that transition into outflowing plumes, resulting in a fjord-scale buoyancy-driven circulation (Carroll et al., 2015; Cowton et al., 2015; Motyka et al., 2003). Similarly, surface runoff or river input can drive a classical estuarine exchange flow (e.g., Geyer & MacCready, 2014). In addition, fjord circulations and fjord/shelf exchanges can be forced by tides, shelf-density fluctuations, and local winds (Cottier et al., 2010; Farmer & Freeland, 1983; Stigebrandt, 2012).

1.2. Dominant Wind Events

There are typically two dominant modes of wind forcing in the vicinity of fjords: local along-fjord winds and along-shore winds on the shelf outside the fjord. In east Greenland, the compression of atmospheric cyclones against Greenland's steep topography causes frequent barrier wind events, characterized by intensified along-shore winds over the shelf ocean (Harden et al., 2011; Moore & Renfrew, 2005). These shelf winds have been found to indirectly drive fjord circulation in southeast Greenland: shelf winds drive shelf-density fluctuations that drive baroclinic flows within the fjords (Harden et al., 2014; Jackson et al., 2014; Straneo et al., 2010; Sutherland et al., 2014b).

Within fjords, winds are typically oriented along the fjord axis and katabatic winds are common (Putnins, 1970). In Sermilik Fjord of southeast Greenland, downslope flow off the ice sheet drives along-fjord wind events, called piteraqs, with a mean speed of 20 m s^{-1} (Oltmanns et al., 2014). These downslope wind events are less frequent but more intense than the shelf barrier winds. Piteraqs have been shown to drive large heat fluxes over the Irminger Sea and offshore transport of sea ice (Oltmanns et al., 2014), but the impact of piteraqs and other katabatic winds on fjords around Greenland is largely unknown and the focus of this study.

1.3. Previous Theories for Wind-Driven Exchange

There is ample evidence that fjords (outside of Greenland) respond to local wind forcing (e.g., Farmer, 1976; Matsuura & Cannon, 1997; Moffat, 2014; Svendsen et al., 2002). Generally, the upper layer is found to move in the direction of the wind, with a return flow at depth. However, there is no general dynamical framework for understanding local wind forcing across different fjords.

Farmer (1976) derived an analytical solution for local wind forcing in narrow fjords, based on a linear two-layer model that neglects rotation and includes a linear parameterization for bottom friction. The model compared well with observations from Alberni Inlet in British Columbia, a fjord whose width is significantly less than the deformation radius (Farmer, 1976; Farmer & Osborn, 1976). Farmer's model was later applied to Puget Sound, both in its original form to examine highly stratified conditions (Matsuura, 1995) and modified as a continuously stratified normal-mode model for weak stratification conditions (Matsuura & Cannon, 1997). In both cases, the model replicated the basic features of the observations.

Svendsen and Thompson (1978) used a reduced version of Farmer's model—assuming a deep lower layer, no viscosity, and a very long fjord—with periodic diurnal wind stress to examine Jøsenfjord in Norway. They find that wind stress dominates over freshwater forcing of the fjord, though the wind response is trapped in the surface layer.

On the numerical modeling side, Klinck et al. (1981) modeled an idealized two-layer fjord/shelf system to examine shelf forcing and local wind forcing—also neglecting rotation by assuming a narrow fjord—and found that surface velocities were in phase with the wind while lower layer velocities were out of phase. More recent numerical modeling studies have used realistic bathymetry and wind (e.g., Kawase & Bang, 2013) to explore wind forcing of individual fjords. However, a general dynamical framework for understanding wind forcing across different fjords is absent.

A more extensive body of work has examined local wind forcing in coastal plain estuaries, often focusing on the wind's importance relative to the estuarine exchange flow (e.g., Geyer, 1997; Hansen & Rattray, 1965) and shelf forcing (e.g., Garvine, 1985; Janzen & Wong, 2002; Wang & Elliott, 1978). The theory and models that have emerged from these studies are derived for shallow systems where the barotropic response is often dominant and horizontal salinity gradients are strong—thus not clearly relevant to deep, stratified fjords.

Nevertheless, several recent fjord studies have drawn upon theory derived for coastal plain estuaries. Moffat (2014) finds that the exchange flow in a Patagonian glacial fjord is modulated by local wind stress, and the nature of this modification can be replicated with theory from Hansen and Rattray (1965). This theory gives a 1-D solution for the velocity based on a balance between stress divergence and pressure gradient, assuming uniform stratification, a constant horizontal density gradient and uniform eddy viscosity—assumptions that are not generally applicable to deep stratified fjords.

Additionally, several recent studies have made a scaling argument based on partially mixed estuaries to assess when local wind forcing should be important in fjords. Sutherland et al. (2014b) and Inall et al. (2015) use the Wedderburn number to suggest that—in a Greenlandic and Norwegian fjord, respectively—the local winds should be an important driver in winter but relatively insignificant in summer. While the original Wedderburn number is the ratio of the wind-driven setup to the mixed layer depth (Monismith, 1986; Spigel & Imberger, 1980), these recent studies use an estuarine variation of the Wedderburn number where the wind-driven setup is scaled relative to the estuarine horizontal density gradient (Geyer, 1997). The applicability of this scaling, however, is untested for fjords.

A general framework for understanding wind forcing across fjords of different geometries and stratifications is lacking. Most theoretical work has focused on fjords that are narrow relative to the deformation radius, yet many fjords in Greenland have widths that are roughly equal to the deformation radius (Jackson, 2016). This leaves open many basic questions about the dynamics of wind forcing and the magnitude of shelf-fjord exchange across the parameter space of fjords, in Greenland and elsewhere.

Here we use a numerical model and theory to investigate the dynamics of wind-driven circulation and exchange across fjords of different geometries and stratifications. Next, we apply the model to the case of Sermilik Fjord, southeast Greenland, where strong along-fjord wind events are known to occur and where existing oceanic data provide the opportunity of a comparison with the theoretical and modeling results.

2. A Model for Wind-Driven Exchange

The general oceanic response to down-fjord winds will be initially explored with a nonlinear numerical model. The configuration is idealized so that the dominant parameters can be easily varied in order to discern their influence on the exchange between the fjord and ocean shelf. The numerical model allows for a wide exploration of parameter space but, in isolation, yields little in the way of insight into the controlling dynamics. Predictions from the model will be compared with simple theoretical ideas in section 3, and the model with more representative wind forcing will be compared with observations in section 4.

2.1. Model Configuration and Forcing

The model is the Massachusetts Institute of Technology general circulation model (MITgcm), Marshall et al. (1997). It solves the hydrostatic, primitive equations of motion on a staggered Cartesian C-grid at fixed depth levels. The domain is set on a *f*-plane, so the Coriolis parameter is constant at $f_0 = 1.2\times10^{-4}\,\mathrm{s}^{-1}$. Subgrid-scale horizontal viscosity A is parameterized by the Smagorinsky (1963) deformation-dependent scheme as

$$A = \left(\frac{\nu\delta}{\pi}\right)^2 D \qquad D = [(u_x - v_y)^2 + (u_y + v_x)^2]^{1/2} \tag{1}$$

where δ is the model grid spacing, $\nu = 2.5$ is a nondimensional coefficient, D is the deformation field, and subscripts indicate partial differentiation. Vertical viscosity and diffusivity are represented with the KPP mixing parameterization (Large et al., 1994) and background mixing coefficients of $10^{-5}\,\mathrm{m}^2\,\mathrm{s}^{-1}$. There is also a quadratic bottom drag with a coefficient of 2.5×10^{-3}. The lateral boundary conditions are no-slip and no normal flux. The model utilizes a linear equation of state such that density is related to the salinity as $\rho = \rho_0 + \alpha_S S$, where $\alpha_S = 0.8\,\mathrm{kg\,m}^{-3}$ is the haline contraction coefficient.

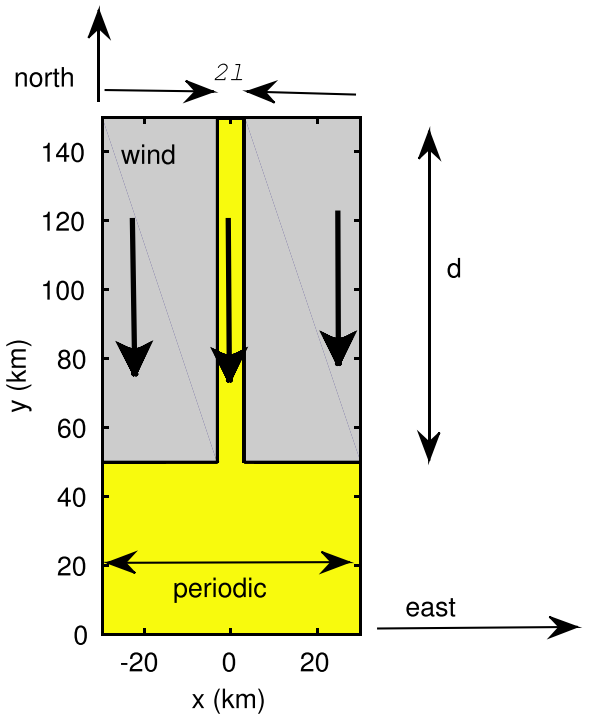

Figure 1. Model domain: periodic channel in east-west, closed northern and southern boundaries. A fjord of length d and width $2l$ is adjacent to an open ocean. The bottom depth is 500 m and flat. A wind that is uniform in space and time is applied at time zero.

The standard model domain is 60 km $\times$ 150 km with a periodic channel in the zonal direction and a rectangular fjord of length $d = 100$ km extending to the northern boundary (Figure 1). (Wider domains were also tested and the results were qualitatively the same as those reported in this section.) For this calculation, the fjord width, defined as $2l$, is 6.25 km, although this will be varied. The model horizontal grid spacing is $\delta = 250$ m and the vertical grid spacing varies between 5 m near the surface and 80 m near the bottom (total of 20 levels). The bottom is flat at $H = 500$ m. In order to keep the problem as simple as possible, the model is forced by a spatially and temporally uniform wind stress to the south. In reality, the winds decay away from the mouth of the fjord in both the zonal and open-ocean directions. Somewhat more realistic winds that include both spatial and temporal variability will be considered in section 4. The initial stratification is approximately two-layer, with an upper layer salinity of 31, a lower layer salinity of 32.5 ($\Delta S = 1.5$) and a hyperbolic tangent transition of half-width 20 m and centered at $h_1 = 150$ m. This gives the thickness of the lower layer as $h_2 = 350$ m. The model domain and stratification are chosen to represent typical conditions during the nonsummer months in Sermilik Fjord, located in southeast Greenland.

This stratification gives a baroclinic deformation radius of $L_d = C/f_0 = 8.3$ km, where $C = (gh_1h_2\alpha_S\Delta S/\rho_0 H)^{1/2} = 1\ \mathrm{m\,s^{-1}}$ is the baroclinic gravity wave speed. The deformation radius is slightly greater than, but similar to, the fjord width, as is typically the case for the fjords of Greenland (Jackson, 2016). The initial state is a resting ocean and a southward wind stress of 1.5 N m^{-2} is abruptly turned on at time zero and held constant for a period of 3 days. This is longer than typical katabatic wind events last, but it is used here in order to better compare the model to the theory in the following section.

2.2. Example of Exchange

The general response of the model to the southward wind stress is outflow in the upper layer and inflow in the lower layer. The cross-fjord averaged meridional velocity at the mouth of the fjord is shown in Figure 2a as a function of depth and time. The outflow is a maximum at the surface, where it exceeds 50 cm s^{-1}, but the entire low-salinity layer is flowing out for most of the simulation. The outflow is maximum after about 1 day and then decreases to nearly zero by day 3. There is a weaker inflow in the lower layer that nearly compensates for the outflow, so the net transport across the mouth of the fjord is close to zero at all times, i.e., the exchange is baroclinic. The average zonal velocity is shown in Figure 2b as a function of time. The zonal velocity is only a weak function of along-fjord distance, at least away from the northern boundary. During the first 2 days, the flow is toward the west near the surface and toward the east in the lower part of the low-salinity layer. The westward flow is a result of the wind stress and the Ekman transport while the deeper flow is below the Ekman layer and partially offsets the deep meridional pressure gradient that results largely from the sea surface height gradient. The transport of low-salinity water out of the fjord, defined as $S < 31.5$, is shown in Figure 2c. The outflow increases rapidly over the first day to its maximum of approximately 3.2 $\times$ 10^5 m^3 s^{-1}, afterward it decreases more slowly toward zero over the following 2 days. The cross-fjord momentum balance is very nearly geostrophic such that the inflowing/outflowing velocity is balanced by the cross-fjord pressure gradient.

It is helpful to consider the balance of terms in the meridional momentum equation in order to develop a more fundamental understanding of what controls the exchange between the fjord and open ocean. The momentum equation solved by the MITgcm can be written as:

$$\underset{\text{tendency}}{v_t} = \underset{\text{nonlinear}}{-uv_x - vv_y - wv_z} \quad \underset{\text{Coriolis}}{+f_0 u} \quad \underset{\text{pressure}}{-P_y/\rho_0} \quad \underset{\text{wind}}{+\tau} \quad \underset{\text{friction}}{+F} \tag{2}$$

where F represents lateral viscosity and bottom drag. In order to get an overall sense of the momentum budgets, these terms will be considered in two ways. The temporal evolution is indicated by their average over the upper layer and over the meridional extent of the fjord, as shown in Figure 3a. Early in the calculation the wind forcing (black line) is partially balanced by the pressure gradient (dark blue), friction (cyan),

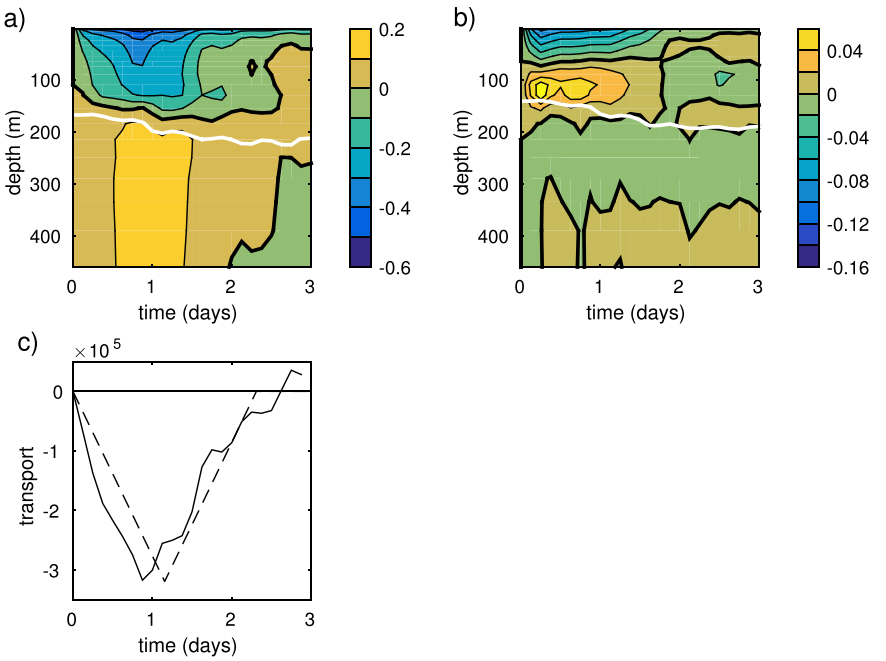

Figure 2. (a) Meridional velocity (m s^{-1}) averaged across the fjord at the mouth as a function of time and depth for the case with uniform winds applied for 3 days. (b) Zonal velocity (m s^{-1}) averaged across the fjord at the mouth as a function of time and depth. (c) Transport (m^3 s^{-1}) of low-salinity upper layer at the mouth of the fjord as a function of time. The solid line is from the numerical model and the dashed line is from the theory of Farmer (1976), discussed in section 3. The white contour in Figures 2a and 2b is the depth of $S = 31.5$, marking the transition between the fresh upper layer and the salty lower layer, and the zero velocity contour is bold.

and the Coriolis term (red). However, this is not sufficient to balance the entire wind stress so the tendency term is negative, indicating flow acceleration to the south. After 1 day, the Coriolis and frictional terms have remained about the same but the pressure gradient has increased sufficiently to balance the wind stress and the flow stops accelerating. The pressure gradient increase is a result of a falling sea surface height at the head of the fjord due to slightly more water being advected out in the upper layer than is advected into the fjord in the deep layer. After that time, the pressure gradient continues to increase, Coriolis and friction decrease and, by the end of the calculation, the pressure and wind are nearly in balance.

The average of the momentum terms in time, depth of the upper layer, and latitude is shown as a function of cross-fjord position in Figure 3b. In the center of the fjord, the primary balance is between the wind stress and pressure gradient. The Coriolis term is working slightly against the wind, but it is much weaker than the

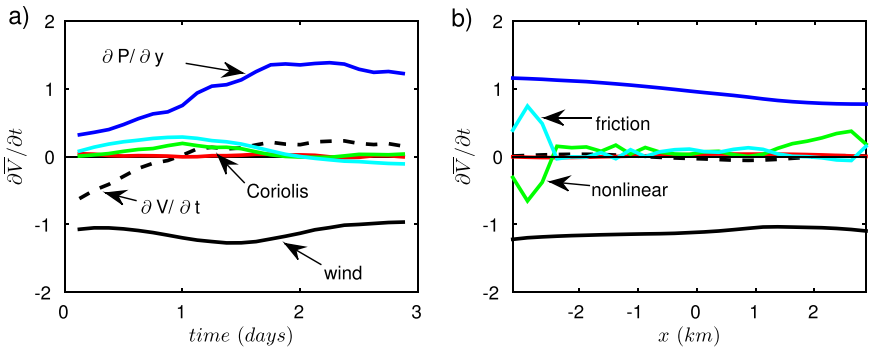

Figure 3. The terms in the meridional momentum equation averaged over the upper layer and in (a) *x* and *y*; (b) *y* and *t* for the run shown in Figure 2. Black: wind; blue: pressure gradient; red: Coriolis; cyan: friction; green: nonlinear advection; and dashed: time-dependence (units 10^{-5} m s^{-2}).

pressure gradient. The tendency term is nearly zero because the flow, after 3 days, is nearly back to its initial state of rest (even though the wind is still being applied).

The frictional term is small everywhere except near the western boundary, while the nonlinear term is significant near both boundaries. The nonlinear term is dominated by the zonal advection of meridional momentum (uv_x). Near the eastern boundary, this results in a net advection of slow water from the eastern viscous boundary layer (recall the no-slip boundary condition) into the interior, so it works to reduce the southward flow. Near the western boundary, it is advecting southward momentum from the interior toward the slower moving water in the western viscous layer, thus increasing its southward momentum. This leads to the narrow and strong viscous boundary layer along the western boundary (cyan line). Thus, while the overall influence of the nonlinear terms is small, they do work to shift momentum dissipation from being symmetric between eastern and western boundaries to being primarily along the western boundary.

3. Theoretical Considerations

The localization of the frictional terms in the upper layer to the side boundary suggests two limits for the balance of terms in the momentum equation. If the fjord is wide compared to the frictional boundary layer width, it is assumed that friction can be ignored and the balance is between wind forcing, the pressure gradient, and time-dependence, although for sufficiently wide fjords it is expected that the Coriolis term may also become important. If the fjord is narrow compared to the viscous boundary layer width, then it is assumed that the Coriolis and pressure gradient terms can be ignored and the balance is between wind forcing and friction. Theoretical estimates for the exchange will now be derived for these two limits and then compared with numerical model calculations.

Consider first the case of a wide fjord. We use the theoretical model developed by Farmer (1976) for a two-layer fjord circulation subject to wind forcing that neglects rotation and friction. Farmer (1976) also considered a linear drag term but this is not appropriate for the present configuration, where the friction is due to the no-slip side wall boundary condition and is predominantly located near the boundaries. For simplicity, we will consider the case of uniform wind, steady in time, of strength $\tau_0 < 0$ that is turned on at time zero over a resting ocean. The Farmer model for this case predicts an along-fjord transport per unit width, ϕ, of

$$\phi(y,t) = \frac{\tau_0 h_2}{\rho_0 H}\int_0^t [-\mathcal{H}(t'-y/C)+0.5\mathcal{H}(t'-(y+d/C))-0.5\mathcal{H}(t'-(d-y)/C)+\mathcal{H}(t')]dt' \tag{3}$$

where $\mathcal{H}$ is the Heaviside step function, $C=(g\alpha_S \Delta S h_1 h_2/\rho_0 H)^{1/2}$ is the baroclinic gravity wave speed, d is the meridional extend of the fjord, and y is the distance from the head of the fjord. The transport predicted by the theory at the mouth of the fjord, where $y = d$, is shown in Figure 2c by the dashed line. The general trend found in the model for this central case is well predicted by the theory. Specifically, there is a nearly linear increase over the first day followed by a decrease back to zero flow. After the wave, signal has traveled back to the head of the fjord, the pressure gradient has developed such that it exactly balances the wind stress and there is no flow in the fjord.

If the exchange is purely baroclinic, a good approximation here, the upper layer averaged velocity is given simply by ϕ/h_1. The maximum layer averaged outflow velocity at the mouth of the fjord, V_m, occurs at time $t_m = d/C$, or the time it takes a wave propagating at C to travel the length of the fjord

$$V_m = \frac{\tau_0 h_2}{2\rho_0 h_1 H}\frac{d}{C}. \tag{4}$$

For the parameters in the numerical example above, $d = 100$ km, $C = 1\,\mathrm{m\,s^{-1}}$, $t_m = 1.15$ days, and $V_m = 0.34\,\mathrm{m\,s^{-1}}$. The maximum outflow velocity increases most strongly with increasing fjord length d, increasing wind stress τ_0, and decreasing baroclinic wave speed C. While (4) will remain qualitatively correct, the phase speed C will be altered by consideration of sloping side walls.

Three additional model calculations were done with $l = 3.125$ km for comparison with the theory (Figure 4). These parameter variations result in changes in the wave speed C and the time for the wave to travel the length of the fjord d/C, and thus the maximum expected velocity and spin-up time. The general trends in the average upper layer velocity in the model compare well with that predicted by the theory, although the

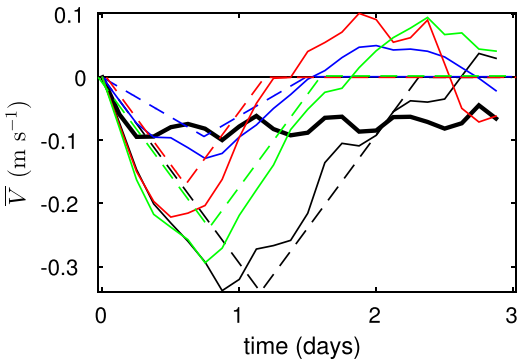

Figure 4. The averaged upper layer velocity at the mouth of the fjord as a function of time with l=3.125 km. Black: central run, as in Figure 2; ΔS=2.5 (green); d=50 km (red); and ΔS=2.5, h_1=250 m (blue), other parameters as in the central case. Solid lines: numerical model; dashed lines: theory (3). Bold black line is as the thin black line with l=625 m.

model maximum velocity is slightly larger than the theory and there is a flow reversal for times greater than $2d/C$. The result for a run with the standard parameters but a fjord width of 1.25 km is given by the bold black line. This narrow run behaves very differently. Instead of reaching a peak and decreasing back to zero, it levels off quickly and remains nearly constant for the duration of the calculation. The dynamics that control this narrow fjord regime are considered next.

A scaling for the width of the frictional boundary layer can be derived by first assuming a balance between wind and viscosity

$$Av_{xx} = \frac{\tau_0}{\rho_0 h_1}. \tag{5}$$

The validity of this assumption will be demonstrated after a scaling for the viscous boundary layer width has been derived. The Smagorinsky (1963) viscosity (1) is a nonlinear parameterization that attempts to represent the downscale cascade of energy from the resolved scale to very small scales, where it is ultimately dissipated. The formulation assumes that as the model grid spacing decreases, the deformation D will increase such that the downscale energy flux, $\varepsilon = AD^2$, remains constant. One could also use the Leith parameterization (Leith, 1996), which assumes an upscale energy cascade and a downscale enstrophy cascade. However, Fox-Kemper and Menemenlis (2008) suggest the Smagorinsky parameterization for model grid spacing much less than the baroclinic deformation radius and $\delta/L_d = 0.03$ here. Analysis similar to what follows has also be done for the Leith parameterization, yielding a similar result, and so the qualitative behavior is not overly sensitive to this choice of parameterization. To estimate A in the real ocean, situations would require knowledge of the energy flux ε and the deformation field D.

For a simple horizontal shear flow with boundary layer width L and a maximum offshore velocity of V_m, $D \approx V_m/L$, and

$$A = \left(\frac{\nu\delta}{\pi}\right)^2 \frac{V_m}{L}. \tag{6}$$

Combining (5) and (6) with (4), the length scale of the boundary layer is

$$L = \left[\left(\frac{\nu\delta}{\pi}\right)^2 \frac{\rho_0 h_1}{\tau_0} V_m^2\right]^{1/3} = \left[\left(\frac{\nu\delta}{2\pi}\right)^2 \frac{\tau_0}{\rho_0 h_1}\left(\frac{dh_2}{CH}\right)^2\right]^{1/3}. \tag{7}$$

For the central case discussed in the previous section, L = 0.8 km. Friction will limit the maximum velocity in the middle of the fjord when $L \geq O(l)$. In that case, the maximum velocity in the middle of the channel, V_0, is

$$V_0 = \left[\left(\frac{\pi}{\nu\delta}\right)^2 \frac{\tau_0}{\rho_0 h_1} l^3\right]^{1/2}. \tag{8}$$

Note that in the viscous limit the velocity reaches a steady state outflow, unlike the inviscid limit in which the wind is balanced by the pressure gradient and there is no flow. This is consistent with the results for the narrow fjord in Figure 4, for which $L/l = 1.3$.

The models of Farmer (1976) and Moffat (2014) used a linear interfacial and bottom drag to parameterize frictional effects. The friction in our model is dominated by lateral viscosity, however, for shallow fjords, it is possible that bottom drag could be more important. For example, the shallow fjord off Patagonia considered by Moffat (2014) has a lower layer thickness of O(50 m) and maximum lower layer velocities of O(0.15 m s^{-1}). Taking a quadratic bottom drag coefficient of $C_d = 0.0025$, this gives a deceleration of $O(10^{-6}$ m s$^{-2})$. This is comparable to the acceleration due to down-fjord winds in that region, but an order of magnitude weaker than the dominant terms in our applications. In general, the ratio of momentum loss due to quadratic bottom drag (F) to the momentum input due to down-fjord wind (W) can be written as

$$\frac{F}{W} = \frac{C_d \tau_0 d^2}{4\rho_0 H^2 C^2} = \frac{C_d \tau_0 d^2}{4\rho_0 g' h_1 h_2 H} \tag{9}$$

where $g' = g\alpha_S \Delta S/\rho_0$ is the reduced gravity between the upper and lower layers. The drag contribution is calculated using a lower layer velocity derived from the inviscid Farmer (1976) theory (equation (4)). For our

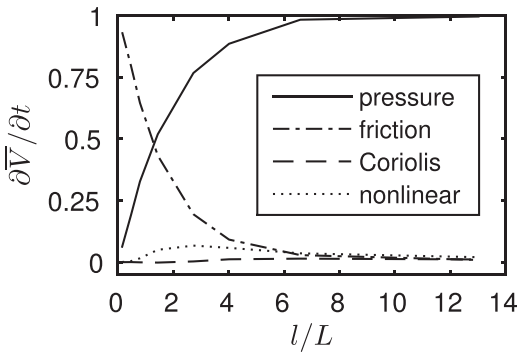

Figure 5. The right-hand side terms in the meridional momentum equation (2), scaled by the magnitude of the wind stress, averaged over the upper layer and in *x*, *y*, and time as a function of *l*/*L*. Time-dependence is negligible and thus not shown.

application, this ratio is $O(10^{-2})$ and bottom drag is negligible. However, bottom drag does become more important for long, shallow, weakly stratified, and strongly forced fjords.

The scaling for the horizontal boundary layer suggests that friction will dominate the right-hand side of (2) when $l \ll L$ and the inviscid theory of Farmer will be appropriate when $l \gg L$. These limits are tested by the relative importance of the terms in the meridional momentum equation, when averaged over the width and length of the fjord in the low-salinity layer, as a function of *l*/*L*. The model was run with the same forcing and stratification as the case discussed above with fjord widths ranging from 125 m to 20.25 km (the grid spacing was reduced to 125 m for the narrowest case). The average value of the terms on the right-hand side of (2), scaled by the wind stress (which is -1 on this scale), is shown in Figure 5. The time-dependence term is negligible and not shown. For wide fjords, the pressure term nearly balances the wind stress, with only small contributions from the Coriolis, frictional, and nonlinear terms. This broadly supports the assumption in the inviscid Farmer theory. Even though the widest fjord width is approximately $2.5L_d$, rotational effects are still small. This is because the westward flow in the Ekman layer is nearly balanced by a return eastward flow in the lower part of the upper layer. Since the Coriolis acceleration is proportional to the net zonal transport in this layer, these eastward and westward flows nearly cancel in their acceleration of the meridional flow. For very narrow fjords, $L/l < O(1)$, the momentum equation reduces to a balance between friction and wind. These results support the two limits derived above for the maximum velocity in the fjord (equations (4) and (8)).

A series of model runs was carried out with the fjord widths varied from 125 m to 20.25 km and different values for τ_0, ΔS, d, and h_1, as summarized in Table 1 (56 runs). The maximum upper layer velocity averaged across the fjord at the mouth was diagnosed from each of these calculations and is plotted against the half-width of the fjord in Figure 6a. The peak velocity ranges from about 2 to about 80 cm s^{-1}. The velocity decreases drastically as the width gets less than 2 km, and also shows a smaller decrease for wide domains. Although these trends are common to each set of runs, there is wide scatter between sets.

The velocity scaled by V_m from (4) is plotted as a function of the fjord half-width scaled by the viscous boundary layer width L in Figure 6b. The two theoretical limits are also indicated on the figure, the dashed line for V_m, which is independent of *l*/*L*, and the solid line is $V_0/2$, the factor of 2 to approximate the cross-fjord average. The calculations broadly follow these two predictions. For $l/L > 1$, the model produces maximum velocities that are 50−105% of V_m, with the lowest values generally for the widest channels. (Note that the results for $l/L > 15$ are all shown at $l/L = 15$ in order to better visualize the results near $l/L = O(1)$.) Although there is some scatter, there is a general tendency for the model to produce velocities in excess of the theory for moderately wide fjords and somewhat below the theory for very wide fjords. Nonetheless, the theory does a pretty good job of collapsing the scatter seen in Figure 6a. For $l/L < O(1)$, the model velocity is reduced much below the inviscid theory but follows fairly closely that predicted by the simple boundary layer scaling (8). The model runs transition from the inviscid theory to the viscous balance for $l/L = O(1)$.

The nondimensional maximum velocity is also plotted against the fjord width scaled by the baroclinic deformation radius in Figure 6c. The decrease in velocity with increasing fjord width is more evident when scaled by the deformation radius compared to the scaling using L, suggesting that the deformation radius is a more relevant length scale in this regime. Although there is not an equivalent to the Farmer theory that includes rotation, it is likely that this reduction in maximum velocity is a result of rotational effects as $2l/L_d > 1$. In the parameter range relevant to Greenland fjords, $2l/L = O(1)$, the inviscid theory is very close to the model results. However, for narrow fjords, there is more scatter between runs than when scaled with L, confirming that the viscous length scale is appropriate for that regime.

A useful quantity to measure the impact of the wind event on the fjord is the total amount of low-salinity water that is fluxed out of the fjord, M. This is simply the integral of the outflowing velocity at the mouth of the fjord over the time period $2t_m$, based on the inviscid theory of Farmer (1976):

Table 1
Parameters for the Model Calculations and Symbols Used in Figures 6 and 7

τ_0 (N m^{-1})	ΔS	d (km)	h_1 (m)	Symbol
1.5	1.25	100	150	□
1.5	2.5	100	150	○
0.15	1.25	100	150	◁
1.5	1.25	100	75	★
1.5	1.25	50	150	◇
1.5	1.25	100	250	△
1.5	2.5	100	250	▷

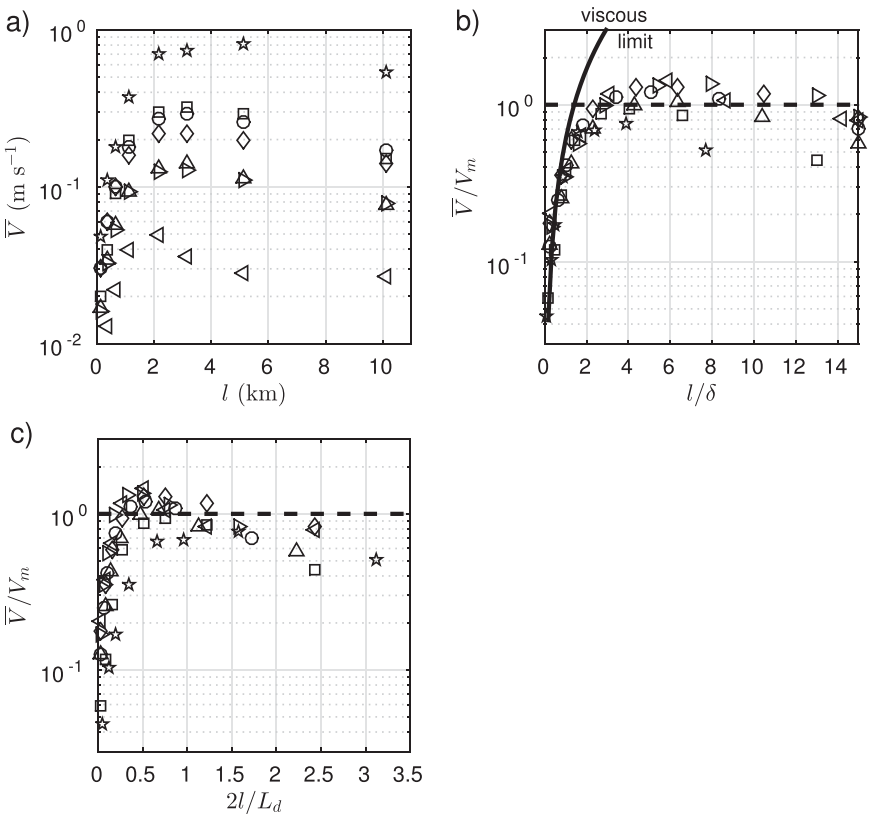

Figure 6. (a) Maximum upper layer velocity at the mouth of the fjord as a function of l for each parameter set in Table 1. (b) Maximum velocity scaled by V_m as a function of l/L. (c) Maximum velocity scaled by V_m as a function of $2l/L_d$. The theoretical predictions for the inviscid and frictional limits are given by the dashed and solid lines. Symbols are for different sets of model parameters, as in Table 1.

$$M = \frac{\tau_0 l h_2}{\rho_0 H}\left(\frac{d}{C}\right)^2 = \frac{\tau_0 l d^2}{g\alpha_S \Delta S h_1}. \tag{10}$$

It is interesting to note that the exchange is independent of the thickness of the lower layer because of C^{-2}. For example, for a decrease in lower layer thickness, the velocity is reduced by a factor of h_2/H but the waves are slower so that the exchange takes place over a longer time period. The exchange found in the model is compared to that predicted by the theory in Figure 7a. The model exchange is the integral of the outflowing velocity where $S < 31.5$ over the time period $2t_m$. For cases with $l/L > 1$ (open symbols), the model and theory compare fairly well, with the theory slightly overpredicting the model exchange for moderately wide fjords. For $l/L < 1$ (solid symbols), the model exchange is generally well below that predicted by the inviscid theory.

The portion of the initial low-salinity layer that gets flushed out of the fjord over a period of 1 day, which is a typical duration of katabatic wind events along east Greenland, is shown in Figure 7b. The trends predicted by the theory are reproduced in the model for the wide fjords and, as expected, the narrow fjords produce much less exchange. The percent exchanged ranges from only about 1% for the cases with weak winds of 0.15 N m^{-2} to almost 40% for the cases with the thinnest upper layer and 1.5 N m^{-2} wind stress. In general, the percent exchange is greater for thin upper layers (as might be found in summer), slow baroclinic wave speeds, strong winds, or short fjords. For the central case discussed above with $\tau = -1.5$ N m^{-2}, $d = 100$ km, $l = 3.125$ km, and $\Delta S = 1.25$ the theory predicts a volume exchange of 1.1×10^{10} m^3 over 1 day of forcing. That is about 12% of the initial upper layer volume in the fjord. The influx in the deep layer represents an exchange of about 5% of that initial volume. The model run for this case produces an exchange of 16% of the initial upper layer volume and about 7% of the initial lower layer volume, similar to but slightly larger than that predicted by the theory.

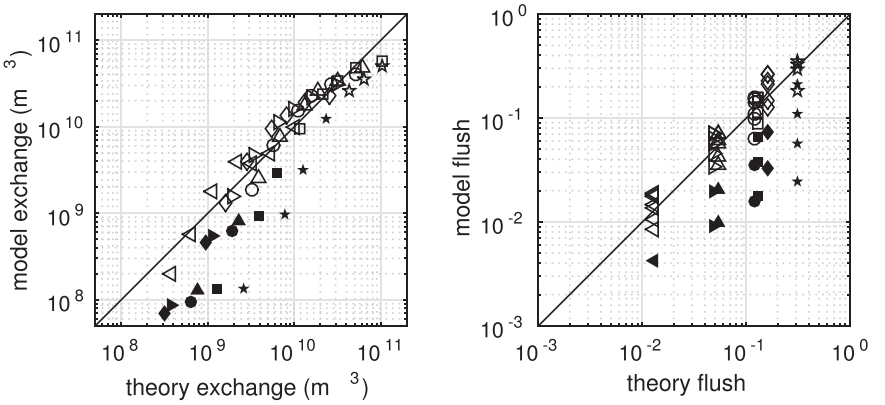

Figure 7. (a) The volume of water with salinity less than 31.5 fluxed out of the fjord from the model and predicted by the theory over time $2d/C$. (b) The amount of the initial volume of low-salinity water in the fjord that is flushed out over 1 day for the model and theory. Symbols are for different sets of model parameters, as in Table 1. Solid symbols are for cases for which $l/L < 1$. The solid line indicates agreement between the model and theory.

4. Observations From Sermilik Fjord

4.1. Setting

The model and theory are compared with observations from Sermilik Fjord, one of the most extensively studied fjords in Greenland (Jackson et al., 2014; Jackson & Straneo, 2016; Straneo et al., 2010, 2011; Sutherland et al., 2014b; Sutherland & Straneo, 2012). Sermilik Fjord is 90 km long, 5–10 km wide, with depths between 500 m and 800 and no shallow sill to impede exchange with the shelf. Helheim glacier, the fifth largest outlet of the Greenland Ice Sheet, drains into the northwest corner of Sermilik Fjord (Enderlin et al., 2014).

The fjord is primarily composed of two water masses from the shelf: warm, salty Atlantic-origin water at depth (>3°) and colder, fresher Polar-origin water above ∼200 m (Straneo et al., 2010). Additionally, glacial runoff and submarine melting create glacially modified water masses in the upper layer (Straneo et al., 2011; Sutherland et al., 2014b). During the nonsummer months, the fjord has a two-layer stratification, with a pycnocline at 150–200 m depth between the Atlantic and Polar water masses, while in the summer the upper layer becomes more stratified and stratification increases toward the surface (Jackson & Straneo, 2016).

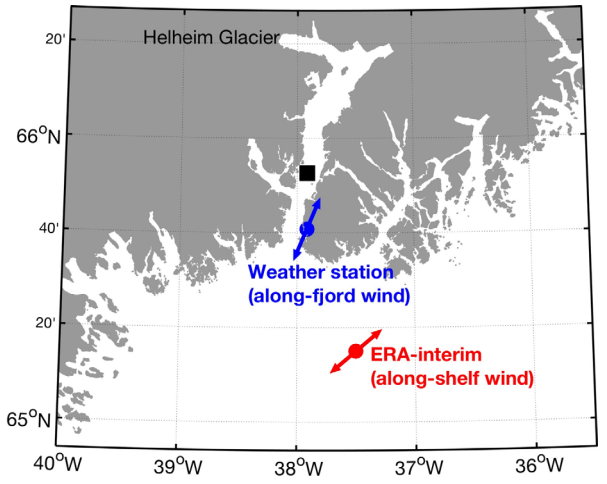

Figure 8. (a) Map of Sermilik Fjord region. The mooring location is shown with a black square. The location of the fjord weather station (used for fjord wind conditions) is shown by the blue dot, and the location of ERA-Interim winds (used for shelf wind conditions) is shown by the red dot. The arrows at the wind locations indicate the principal axis of the wind velocity field at those points. The velocity component along the principal axis is used to capture the along-fjord and along-shelf winds from the fjord weather station and ERA-Interim, respectively.

The primary drivers of circulation also evolve seasonally. In the nonsummer months, shelf-density fluctuations, primarily driven by along-shore shelf winds, drive synoptic variability in the fjord and significant fjord-shelf exchange (Jackson et al., 2014). In the summer, shelf forcing is reduced, and a mean buoyancy-driven exchange flow emerges (Jackson & Straneo, 2016). The fjord is also subjected to occasional strong down-fjord wind events, primarily in the nonsummer months (Oltmanns et al., 2014), and it has been suggested that they contribute to driving fjord circulation (Sutherland et al., 2014a) but their role has not yet been thoroughly investigated.

4.2. Data: Fjord Velocity and Winds

Here we use a midfjord mooring from Sermilik Fjord, deployed from August 2011 to June 2012 and September 2012 to August 2013, to investigate the fjord response to local wind forcing (Figure 8). These records are described extensively in Jackson et al. (2014) and Jackson and Straneo (2016). CTDs were deployed at five depths between 14 and 541 m in 2011–2012 and from 50 to 567 m in 2012–2013. An upward-facing 75 kHz ADCP recorded velocity in 10 m bins over 37–397 m depth in the first year and in 15 m bins over 54–411 m depth in the second year.

Two wind products are used to investigate the wind forcing of the fjord. A weather station on the southeast coast of the fjord (Figure 8) is used to estimate the local wind forcing within the fjord (Hasholt et al., 2004; Oltmanns

et al., 2014). At this weather station, the winds are primarily directed along-fjord, and we use the principal component of the wind velocity to represent the along-fjord component of the fjord winds (orientation of arrows in Figure 8). The ERA-Interim reanalysis, which has been shown to accurately capture winds along the southeast coast of Greenland (Harden et al., 2011), was used to examine the shelf winds offshore of Sermilik Fjord. The ERA wind field at a point 45 km offshore of the fjord's mouth was used to extract a time series of along-shore wind (Figure 8).

In order to compare with the model and theory, we convert wind velocity to wind stress. For the ERA shelf winds, we used the reanalysis wind field at 10 m above sea level with the Large and Pond (1981) formulation. The conversion for the fjord weather station involves more uncertainty because the weather station recorded velocity at 2 m above land on a rocky hill next to the fjord, which is 25 m above sea level. Here we use the Large and Pond (1981) formulation assuming a 2 m height above sea level (i.e., neglecting the difference in drag between the land and ocean). However, there is significant uncertainty in the magnitude of this wind stress estimate; for example, if we instead used a height of 25 m over sea level, the winds stress would be reduced by approximately 40%. Additionally, the presence of icebergs and sea ice in the fjord should alter the effective wind stress. Thus, the overall magnitude of the wind stress from the weather station should be considered a rough estimate. The inviscid theory predicts that the exchange scales linearly with the wind stress, so this uncertainty in the wind stress maps directly onto uncertainty in the exchange.

4.3. Analysis

4.3.1. Composite

To examine the fjord response to down-fjord wind forcing, we create composites of the wind and velocity fields (Figure 9). Eight events over the 2 year moored records are selected based on a criteria for the local

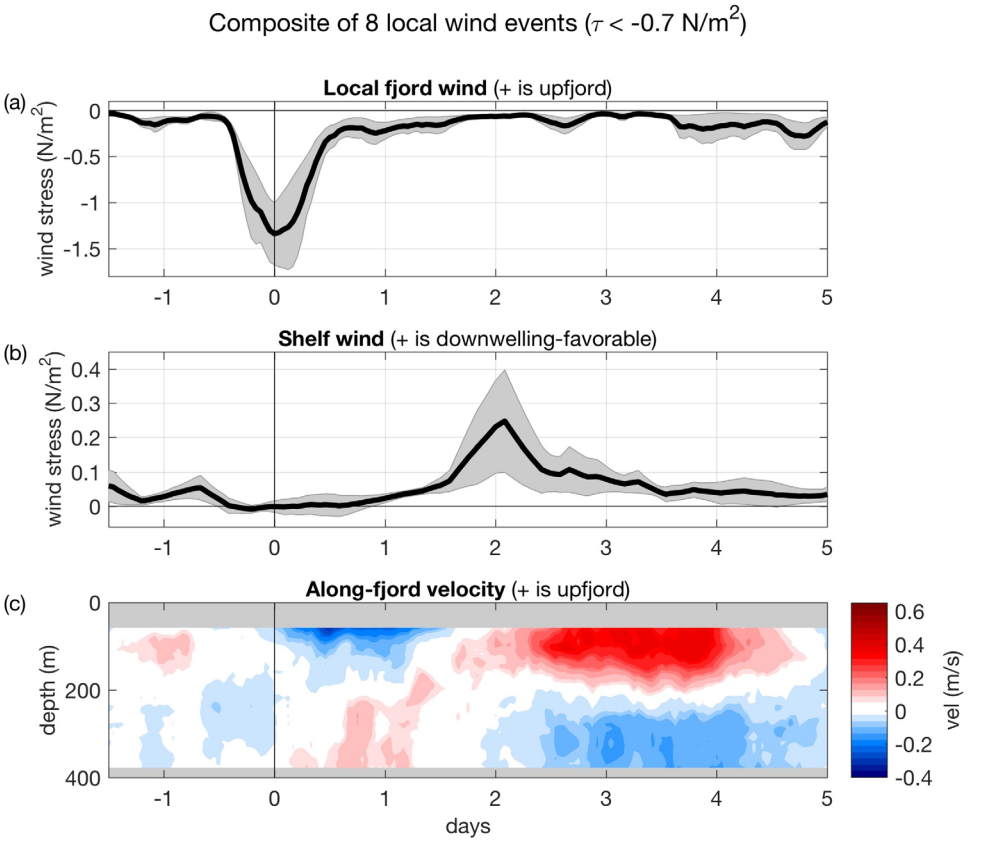

Figure 9. Composite of eight local wind events with down-fjord winds greater than 0.7 N m^{-2}. All fields are aligned and then averaged such that 0 days is the peak wind stress. Error bars are ±1 standard error on the mean. (a) Local wind from weather station, along-fjord component. (b) Along-shelf wind from ERA-Interim; positive is to the southwest and downwelling favorable. (c) Along-fjord velocity at midfjord mooring from 57 to 377 m (depth range covered by ADCP records in both years).

wind stress of $\tau_f < -0.7$ N m^{-2}, where negative wind stress is down-fjord, and the fields are averaged after aligning by the time of maximum wind. This criteria is equivalent to a wind speed criteria of 16 m s^{-1}, which is slightly lower than the 17.4 m s^{-1} threshold used to identify katabatic wind events in Oltmanns et al. (2014). In the 2 years of focus here, there were only 4 events/yr, whereas Oltmanns et al. (2015) find an average of 7.8 events/yr over 1998–2010. In the composite (Figure 9a), the peak wind is 1.3 ± 0.3 N m^{-2} and the wind event lasts approximately 1 day. About 2 days later there is a weaker, downwelling favorable along-shelf wind stress of about 1 day in duration (Figure 9b), although this feature is not present in several of the individual events. We test the sensitivity to this feature by running the model with and without this along-shelf wind. Note that this shelf wind is much weaker than full barrier wind events, which have typical wind stresses of 0.8 N m^{-2} (Harden et al., 2011; Jackson et al., 2014).

The full velocity response is shown as a function of depth and time in Figure 9c. There is outflow in the upper layer that peaks 0.5–1 day after the maximum wind at approximately 0.3 ± 0.1 m s^{-1}. It is likely that the peak outflow velocity is above the depth range of the ADCP. Below 200 m, a weak inflow is observed. This vertical structure is broadly consistent with that found in the model (e.g., see Figure 2a). After 2 days, the velocity at all depths reverses. In the upper layer, the inflow at day 3 is stronger, and more uniform in depth, than the preceding outflow.

We now run the model forced with a typical down-fjord wind event based on this composite. A favorable comparison with the observations will lend support to the model physics, the idealized configuration, and the interpretations in the previous section. The model was run with a 100 km long, 7.5 km wide fjord but in a domain that was extended to 375 km in the along-shelf direction with grid spacing of 250 m in the fjord that gradually expanded to 4 km for distances greater than 90 km from the fjord. The model was forced with a down-fjord wind that was uniform within the fjord but decayed away from the mouth of the fjord over the shelf in both the zonal and meridional directions, as indicated in Figure 10a. (Calculations with a spatially uniform meridional wind produced a similar exchange.) The model wind also varied as a Gaussian in time with a temporal decay scale of 0.5 days and a peak wind stress of -1.3 N m^{-2} at 1 day (Figure 10b). The model was run with just the down-fjord wind, and a second calculation was done with an additional

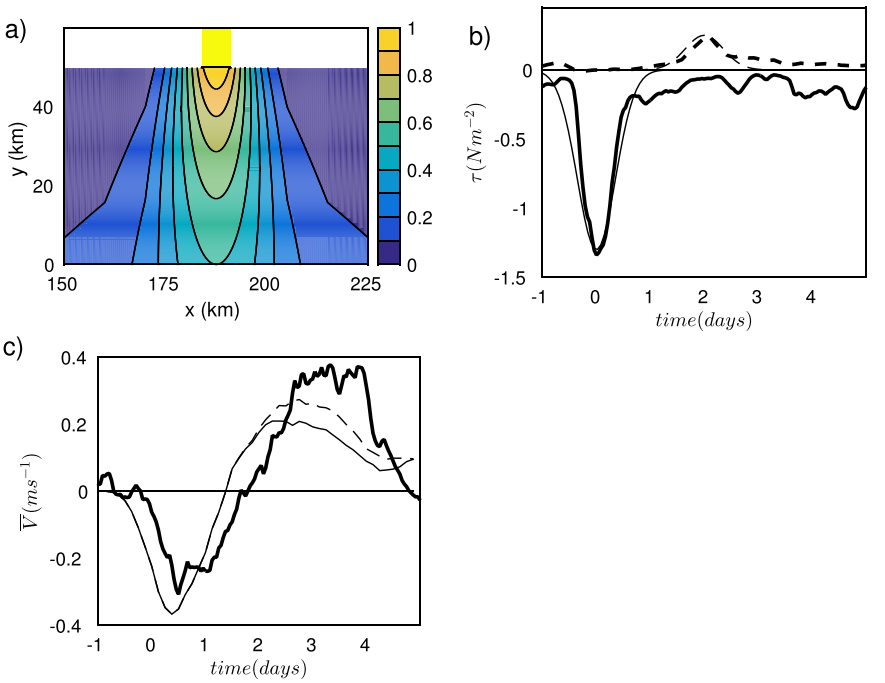

Figure 10. (a) Spatial pattern of wind stress over the shelf in the vicinity of the fjord mouth. (b) Model wind stress (thin lines) for the meridional (solid) and zonal (dashed) wind components. Bold lines are the composite estimates based on the weather station and ERA-Interim locations shown in Figure 8. (c) Along-fjord velocity for the model at mid-fjord and 55 m depth (thin lines) and mooring observations (bold line). The thin solid line is for a calculation with only meridional winds and the thin dashed includes the added along-shelf wind that follows the down-fjord wind (dashed line in Figure 10b).

weaker, spatially uniform along shelf wind with amplitude 0.25 N m^{-2} and Gaussian decay of 0.5 days that peaks on model day 3, 2 days after the peak down-fjord wind (Figure 10b, dashed line).

The model velocity at 55 m depth in the middle of the channel, 25 km from the mouth of the fjord, is shown in Figure 10c. The amplitude and duration of the model outflow are close to the mooring measurements, with a slightly earlier phase. The model also produces an inflow following the outflow event, although the amplitude is only about 60% as strong as the observed inflow. The along-shelf wind event results in a slightly stronger and longer inflow but is otherwise similar to the case with just the down-fjord wind.

4.3.2. Volume Exchanged

We are interested in the exchange between the fjord and shelf that is driven by these along-fjord wind events. The volume flux exchange is estimated in several ways. Due to the limited coverage of the ADCP near the surface, estimates of volume flux have significant uncertainty. First, we estimate the average upper layer volume flux using the composite of velocity at 57 m, assuming no cross-fjord shear, a fjord width of 7.5 km, and an upper layer thickness of 150 m. With this method, the peak volume flux during the outflow is $3.5\pm1.3\times10^5$m^3 s^{-1} and the total volume exchanged (at the midfjord mooring location) is 2.9×10^{10}m^3 over 1.8 days.

Better estimates of volume flux can be calculated in the first year of the record, when the ADCP extended closer to the surface. A time series of upper layer volume flux for this record was calculated in Jackson et al. (2014) by integrating the velocity above the $\sigma = 27$ kg m^{-3} isopycnal and using four methods of extrapolating to the surface. Using this time series of upper layer volume flux, we find that in the first winter, the two largest wind events (with wind stresses of 0.9 and 1.1 N m^{-2}) resulted in peak upper layer volume fluxes of $3.4\pm0.6\times10^5$ and $3.7\pm0.6\times10^5$m^3 s^{-1}, and total volume exchanges of $3.9\pm0.8\times10^{10}$m^3 over 2.2 days and $5.8\pm1.0\times10^{10}$m^3 over 2.3 days. The error bars for these volume fluxes are the spread from using a range of extrapolations, as described in Jackson et al. (2014). The peak outflow in the model is 2.6×10^5 m^3 s^{-1}, similar to but weaker than the observed exchange, while the total volume fluxed out in the model with the along-shelf winds was 2.4×10^{10} m^3.

When compared to the total volume of the upper layer (1.2×10^{11}m^3), the range of values above represent an exchange of 17–35% of the entire upper layer of the fjord during one wind event. Assuming the same volume exchanged in the lower layer (i.e., a purely baroclinic flow) and a lower layer volume of 2.8×10^{11} m^3, there would be an exchange of 7–15% of the lower layer. The model calculation above produced an exchange of 21% of the initial upper layer volume and 9% of the initial lower layer volume, at the lower end but within the observational estimates.

It should be noted that these volume exchanges are recorded at the midfjord mooring location. The velocities are expected to be larger at the mouth of the fjord, so these can be understood as a lower bound on the volume exchanged between the fjord and shelf.

Previous work has shown that the shelf-driven flows in Sermilik drive a typical exchange of $8.5 \pm 0.8 \times 10^{10}$ m^3 over one event—equivalent to 50% of the upper layer volume. Thus these local wind-driven exchanges are smaller but similar in magnitude to the shelf-driven events. However, there are approximately 16 shelf-driven events per year (Jackson et al., 2014) versus 4–8 along-fjord wind events per year (as defined here and in Oltmanns et al. (2014)). Thus, overall in Sermilik the shelf forcing should have a larger impact on exchange and flushing.

5. Sill Influence

Although there is no prominent sill located at the mouth of the Sermilik Fjord, sills are present in other Greenland fjords, such as Godthåbsfjord (Mortensen et al., 2011) and Ilulissat Icefjord (Schumann et al., 2012) along west Greenland, and they may block the exchange between the fjord and shelf. The inviscid Farmer (1976) theory is not readily extended to include bottom topography that is a function of the along-fjord distance. However, the theory can be used to test a simple assumption about how the sill might influence the exchange. If it is assumed that the sill is sufficiently narrow that the wave speed is controlled by the depth of the lower layer away from the sill, C would be determined by the flat-bottom fjord with a lower layer thickness of h_2. This means that the time for waves to propagate from the head to the mouth of the fjord would be independent of the sill depth. However, if it is assumed that the exchange driven locally by

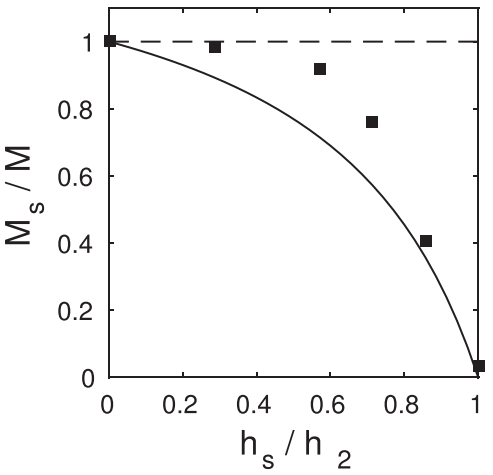

Figure 11. The volume fluxed out of the fjord for a series of model calculations, normalized by the flat bottom exchange, as a function of the fractional sill height h_s compared to the resting lower layer thickness h_2 (symbols). The lines are predictions from the inviscid theory with no sill (dashed line) and where the phase speed is unaffected by the sill but the exchange is controlled by the thickness of layer 2 over the sill, equation (11) (solid line).

the wind and pressure gradient is controlled by the local layer thicknesses h_1 and h_2-h_s, where h_s is the sill height above the flat bottom, then (10) predicts that the outflow volume depends on the thickness of the lower layer at the sill as

$$M_s = \frac{\tau_0 l\,(h_2-h_s)}{\rho_0\,(h_1+h_2-h_s)}\left(\frac{d}{C}\right)^2, \tag{11}$$

where $C=(gh_1h_2\alpha_S\Delta S/\rho_0 H)^{1/2}$ is based on the flat bottom lower layer thickness h_2.

The model was run forced by the composite wind event that includes both the down-fjord and the along shelf winds and a sill located at the mouth of the fjord. The height of the sill above the bottom was varied from 100 to 350 m. The tallest sill corresponds to topography that extends from the bottom to the resting interface between the upper and lower layers.

The volume of upper layer water that flows out of the fjord, normalized by the flat bottom exchange, is shown in Figure 11 as a function of the fractional sill height. The flat bottom solution is indicated by the dashed line and the simple sill representation (11) is given by the solid line. For moderate sill heights, the exchange is close to that predicted by the flat bottom theory. However, the exchange rapidly drops for sill heights greater than about 75% of the resting lower layer thickness, roughly following the heuristic model in which the local exchange is limited by the local lower layer thickness.

The overturning circulation is shown in Figure 12 for the flat bottom case and for the case with $h_s = 300$ m. The overturning circulation over the flat portion of the fjord with a sill is essentially the same as for the case with no sill. As the lower layer thins over the topography, the outflowing waters in the upper layer downwell, resulting in an overturning circula-

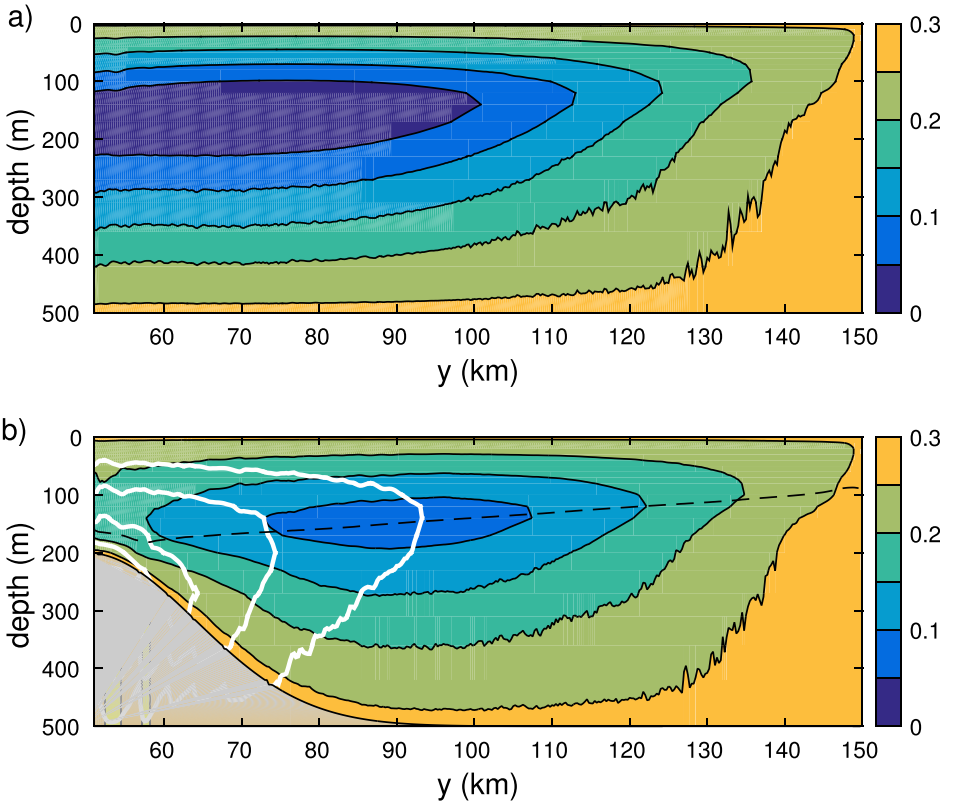

Figure 12. The overturning stream function (10^6 m^3 s^{-1}) at the time of maximum exchange (1.375 days) for: (a) a flat bottom and (b) a 300 m tall sill. The difference between the flat bottom overturning and the sill over turning is shown in Figure 12b by the white contours (contour interval 0.05 10^6 m^3 s^{-1}). The black dashed line in Figure 12b is the mean position of the 31.5 salinity contour, roughly marking the transition from the upper to lower layers.

tion within the fjord. The deep inflow, and hence the upper layer outflow, is eventually shut down for a sill height that extends to the base of the upper layer. It seems possible that hydraulic controls to the exchange may become important as the lower layer becomes very thin at the crest of the sill, but such conditions have not been explored here.

6. Summary

An idealized numerical model, two-layer and scaling theory, and observations have been used to address how much exchange between a fjord and the ocean shelf is expected from katabatic wind events. The numerical model is used to identify two primary regimes. For fjord widths narrow compared to a frictional boundary layer thickness, which depends on the frictional parameterization used, the exchange is limited by lateral friction. For the nonlinear Smagorinsky parameterization used here, the boundary layer width depends on the wind stress, stratification, and fjord length, as well as on the model grid spacing and an empirical constant. For fjords wider than this frictional length scale, the flow is well approximated by the two-layer, nonrotating inviscid theory of Farmer (1976), although the model does show a slight decrease in exchange for fjords much wider than the baroclinic deformation radius, suggesting that rotational effects can become important. This theory predicts that the exchange is largest for fjords with a thin upper layer, slow baroclinic wave speeds, strong winds, or long along-fjord dimensions. A typical wind event will result in an exchange of $O(10\%)$ of the initial low-salinity upper layer between the fjord and shelf. The presence of a sill reduces the exchange only for sills that penetrate most of the way through the lower layer.

The model and theory are used to investigate the response of Sermilik Fjord, SE Greenland, which is known to experience strong along-fjord wind events—whose contribution to the fjord dynamics is currently unknown. A meteorological station in Sermilik Fjord (southeast Greenland) and ERA-Interim reanalysis were used to derive a representative katabatic wind event based on 8 events over a 2 year period. The dominant forcing for these events is the along-fjord katabatic wind with wind stresses exceeding 1 N m^{-2}. An idealized numerical model forced with such winds produces an outflow in the upper layer of $O(30\ cm\ s^{-1})$ in the days following the katabatic wind that is followed by a similar strength inflow over several additional days. Mooring observations collected from Sermilik Fjord, averaged over these eight individual wind events, show a very similar pattern and strength of outflow during/immediately after the katabatic wind followed by a substantial inflow for 2–3 days after that. Although the model exchange is weaker than observed, given the large uncertainties in the wind stress experienced by the fjord and the extrapolation required to estimate the near surface velocities from the observations, we conclude that the model results are broadly consistent with the observed exchange resulting from down-fjord wind events. These results indicate that katabatic wind events represent a significant exchange mechanism between the fjord and shelf for flushing the upper layer of the fjord (where glacial meltwater can accumulate) and renewing the warm, salty waters at depth. However, the shelf wind-driven flows are stronger and more frequent and should have a larger impact on the total exchange and flushing.

Acknowledgments
M.A.S. was supported by the National Science Foundation under grant OCE-1533170. R.H.J. was supported by the NOAA Climate and Global Change Postdoctoral Fellowship. F.S. was supported by the National Science Foundation grants OCE-1434041 and PLR-1418256. The data from Sermilik Fjord are archived at http://accession.nodc.noaa.gov, accession 126772 (2011–2012) and 127325 (2012–2013).

References

Bamber, J., van den Broeke, M., Ettema, J., Lenaerts, J., & Rignot, E. (2012). Recent large increases in freshwater fluxes from Greenland into the North Atlantic. *Geophysical Research Letters*, *39*, L19501. https://doi.org/10.1029/2012GL052552

Carroll, D., Sutherland, D. A., Shroyer, E. L., Nash, J. D., Catania, G. A., & Stearns, L. A. (2015). Modeling turbulent subglacial meltwater plumes: Implications for fjord-scale buoyancy-driven circulation. *Journal of Physical Oceanography*, *45*, 2169–2185.

Cottier, F. R., Nilsen, F., Skogseth, R., Tverberg, V., Skarhamar, J., & Svendsen, H. (2010). Arctic fjords: A review of the oceanographic environment and dominant physical processes. *Geological Society, London, Special Publications*, *344*, 35–50.

Cowton, T., Slater, D., Sole, A., Goldberg, D., & Nienow, P. (2015). Modeling the impact of glacial runoff on fjord circulation and submarine melt rate using a new subgrid-scale parameterization for glacial plumes. *Journal of Geophysical Research: Oceans*, *120*, 796–812. https://doi.org/10.1002/2014JC010324

Enderlin, E. M., Howat, I. M., Jeong, S., Noh, M.-J., Van Angelen, J. H., & van den Broeke, M. R. (2014). An improved mass budget for the Greenland ice sheet. *Geophysical Research Letters*, *41*, 866–872. https://doi.org/10.1002/2013GL059010

Farmer, D. M. (1976). The influence of wind on the surface layer of a stratified inlet: Part II. Analysis. *Journal of Physical Oceanography*, *6*, 941–952.

Farmer, D. M., & Freeland, H. (1983). The physical oceanography of fjords. *Progress in Oceanography*, *12*, 147–122.

Farmer, D. M., & Osborn, T. (1976). The influence of wind on the surface layer of a stratified inlet: Part I. Observations. *Journal of Physical Oceanography*, *6*, 931–940.

Fox-Kemper, B., & Menemenlis, D. (2008). Can large eddy simulation techniques improve mesoscale rich ocean models? *AGU Monograph Ocean Modeling in an Eddyine Regime*, *177*, 319–337.

Garvine, R. W. (1985). A simple model of estuarine subtidal fluctuations forced by local and remote wind stress. *Journal of Geophysical Research*, *90*(C6), 11945–11948.

Geyer, W. R. (1997). Influence of wind on dynamics and flushing of shallow estuaries. *Estuarine Coastal and Shelf Science*, *44*, 713–722.

Geyer, W. R., & MacCready, P. (2014). The estuarine circulation. *Annual Review of Fluid Mechanics*, *46*, 175–197.
Gillard, L. C., Hu, X., Myers, P. G., & Bamber, J. L. (2016). Meltwater pathways from marine terminating glaciers of the Greenland ice sheet. *Geophysical Research Letters*, *43*, 10873–10882. https://doi.org/10.1002/2016GL070969
Hansen, D. V., & Rattray, M. J. (1965). Gravitational circulation in straits and estuaries. *Journal of Marine Research*, *23*, 104–122.
Harden, B. E., Renfrew, I. A., & Petersen, G. N. (2011). A climatology of wintertime barrier winds off Southeast Greenland. *Journal of Climate*, *24*, 4701–4717.
Harden, B. E., Straneo, F., & Sutherland, D. (2014). Moored observations of synoptic and seasonal variability in the East Greenland Coastal Current. *Journal of Geophysical Research: Oceans*, *119*, 8838–8857. https://doi.org/10.1002/2014JC010134
Hasholt, B., Hansen, B. U., Humlum, O., & Mernild, S. H. (2004). Meteorological stations at the Sermilik Station, Southeast Greenland: Physical environment and meteorological observations 2002. *Danish Journal of Geography*, *104*(2), 47–58.
Hellmer, H. H., & Olbers, D. J. (1989). A two-dimensional model for the thermohaline circulation under and ice shelf. *Antarctic Science*, *1*, 325–336.
Holland, D. M., Thomas, R. H., de Young, B., Ribergaard, M. H., & Lyberth, B. (2008). Acceleration of Jakobshavn Isbræ triggered by warm subsurface ocean waters. *Nature Geoscience*, *1*(10), 659–664.
Inall, M. E., Nilsen, F., Cottier, F. R., & Daae, R. (2015). Shelf/fjord exchange driven by coastal-trapped waves in the Arctic. *Journal of Geophysical Research: Oceans*, *120*, 8283–8303. https://doi.org/10.1002/2015JC011277
Jackson, R. H. (2016). *Dynamics of Greenland's glacial fjords* (PhD thesis). Cambridge, MA: Massachusetts Institute of Technology & Woods Hole Oceanographic Institution.
Jackson, R. H., & Straneo, F. (2016). Heat, salt, and freshwater budgets for a glacial fjord in Greenland. *Journal of Physical Oceanography*, *46*(9), 2735–2768.
Jackson, R. H., Straneo, F., & Sutherland, D. A. (2014). Externally forced fluctuations in ocean temperature at Greenland glaciers in non-summer months. *Nature Geoscience*, *7*(7), 503–508.
Janzen, C. D., & Wong, K. C. (2002). Wind-forced dynamics at the estuary-shelf interface of a large coastal plain estuary. *Journal of Geophysical Research*, *107*(C10), 3138. https://doi.org/10.1029/2001JC000959
Jenkins, A. (2011). Convection-driven melting near the grounding lines of ice shelves and tidewater glaciers. *Journal of Physical Oceanography*, *41*(12), 2279–2294.
Kawase, M., & Bang, B. (2013). Seasonal variability of salinity and circulation in a silled estuarine fjord: A numerical model study. *Continental Shelf Research*, *71*(C), 109–126.
Klinck, J., O'brien, J., & Svendsen, H. (1981). Simple model of fjord and coastal circulation interaction. *Journal of Physical Oceanography*, *11*(12), 1612–1626.
Large, W. G., McWilliams, J. C., & Doney, S. C. (1994). Oceanic vertical mixing: A review and a model with a nonlocal boundary layer parameterization. *Review Geophysics*, *32(4)*, 363–403.
Large, W. G., & Pond, S. (1981). Open ocean momentum flux measurements in moderate to strong winds. *Journal of Physical Oceanography*, *11*, 324–336.
Leith, C. E. (1996). Stochastic models of chaotic systems. *Physica D*, *98*, 481–491.
Luckman, A., Benn, D. I., Cottier, F., Bevan, S., Nilsen, F., & Inall, M. E. (2015). Calving rates at tidewater glaciers vary strongly with ocean temperature. *Nature Communications*, *6*, 8566.
Mankoff, K. D., Straneo, F., Cenedese, C., Das, S. B., Richards, C. G., & Singh, H. (2016). Structure and dynamics of a subglacial plume in a Greenland fjord. *Journal of Geophysical Research: Oceans*, *121*, 8670–8688. https:doi.org/10.1002/2016JC011764
Marshall, J., Hill, C., Perelman, L., & Adcroft, A. (1997). Hydrostatic, quasi-hydrostatic, and non-hydrostatic ocean modeling. *Journal of Geophysical Research*, *102*(C3), 5733–5752.
Matsuura, H. (1995). An application of a two-layer model to wind driven sub-tidal currents in Puget Sound. *Journal of Oceanography*, *51*, 571–584.
Matsuura, H., & Cannon, G. A. (1997). Wind effects on sub-tidal currents in Puget Sound. *Journal of Oceanography*, *53*, 53–66.
Moffat, C. (2014). Wind-driven modulation of warm water supply to a proglacial fjord, Jorge Montt Glacier, Patagonia. *Geophysical Research Letters*, *41*, 3943–3950. https://doi.org/10.1002/2014GL060071
Monismith, S. G. (1986). An experimental study of the upwelling response of stratified reservoirs to surface shear stress. *Journal of Fluid Mechanics*, *171*, 407–439.
Moore, G., & Renfrew, I. (2005). Tip jets and barrier winds: A QuikSCAT climatology of high wind speed events around Greenland. *Journal of Climate*, *18*(18), 3713–3725.
Mortensen, J., Lennert, K., Bendtsen, J., & Rysgaard, S. (2011). Heat sources for glacial melt in a sub-Arctic fjord (Godthåbsfjord) in contact with the Greenland Ice Sheet. *Journal of Geophysical Research*, *116*, C01013. https://doi.org/10.1029/2010JC006528
Motyka, R. J., Hunter, L., Echelmeyer, K., & Connor, C. (2003). Submarine melting at the terminus of a temperate tidewater glacier, LeConte Glacier, Alaska, USA. *Annals of Glaciology*, *36*, 57–65.
Motyka, R. J., Truffer, M., Fahnestock, M., Mortensen, J., Rysgaard, S., & Howat, I. (2011). Submarine melting of the 1985 Jakobshavn Isbræ floating tongue and the triggering of the current retreat. *Journal of Geophysical Research*, *116*, F01007. https://doi.org/10.1029/2009JF001632
Oltmanns, M., Straneo, F., Moore, G. W. K., & Mernild, S. H. (2014). Strong downslope wind events in Ammassalik, Southeast Greenland. *Journal of Climate*, *27*(3), 977–993.
Putnins, P. (1970). The climate of Greenland. In S. Orvig (Ed.), *Climate of the polar regions* (pp. 3–113). New York, NY: American Elsevier Publishing Company.
Schumann, K., Völker, D., & Weinrebe, W. (2012). Acoustic mapping of the Ilulissat Ice Fjord mouth, west Greenland. *Quaternary Science Reviews*, *40*, 78–88.
Sciascia, R., Straneo, F., Cenedese, C., & Heimbach, P. (2013). Seasonal variability of submarine melt rate and circulation in an East Greenland fjord. *Journal of Geophysical Research: Oceans*, *118*, 2492–2506. https://doi.org/10.1002/jgrc.20142
Shepherd, A., Ivins, E. R., A, G., Barletta, V. R., Bentley, M. J., Bettadpur, S., . . . Zwally, H. J. (2012). A reconciled estimate of ice-sheet mass balance. *Science*, *338*(6111), 1183–1189.
Smagorinsky, J. (1963). General circulation experiments with the primitive equations: I. The basic experiment. *Monthly Weather Review*, *91*, 99–164.
Spigel, R. H., & Imberger, J. (1980). The classification of mixed-layer dynamics of lakes of small to medium size. *Journal of Physical Oceanography*, *10*, 1104–1121.

Stigebrandt, A. (2012). Hydrodynamics and circulation of fjords. In L. Bengtsson, R. Herschy & R. Fairbridge (Eds.), *Encyclopaedia of lakes and reservoirs* (pp. 327–344). Dordrecht, The Netherlands: Springer Science.

Straneo, F., & Cenedese, C. (2015). The dynamics of Greenland's glacial fjords and their role in climate. *Annual Review of Marine Science*, *7*, 89–112.

Straneo, F., Curry, R. G., Sutherland, D. A., Hamilton, G. S., Cenedese, C., Våge, K., & Stearns, L. A. (2011). Impact of fjord dynamics and glacial runoff on the circulation near Helheim glacier. *Nature Geoscience*, *4*(5), 322–327.

Straneo, F., Hamilton, G. S., Sutherland, D. A., Stearns, L. A., Davidson, F., Hammill, M. O. . . . Rosing-Asvid, A. (2010). Rapid circulation of warm subtropical waters in a major glacial fjord in East Greenland. *Nature Geoscience*, *3*(3), 1–5.

Straneo, F., & Heimbach, P. (2013). North Atlantic warming and the retreat of Greenland's outlet glaciers. *Nature Communications*, *504*(7478), 36–43.

Sutherland, D. A., Roth, G. E., & Hamilton, G. (2014a). Quantifying flow regimes in a Greenland glacial fjord using iceberg drifters. *Geophysical Research Letters*, *41*, 8411–8420. https://doi.org/10.1002/2014GL062256

Sutherland, D. A., & Straneo, F. (2012). Estimating ocean heat transports and submarine melt rates in Sermilik Fjord, Greenland, using lowered acoustic Doppler current profiler (LADCP) velocity profiles. *Annals of Glaciology*, *53*(60), 50–58.

Sutherland, D. A., Straneo, F., & Pickart, R. S. (2014b). Characteristics and dynamics of two major Greenland glacial fjords. *Journal of Geophysical Research: Oceans*, *119*, 3767–3791. https://doi.org/10.1002/2013JC009786

Svendsen, H., Beszczynska-Möller, A., Hagen, J. O., Lefauconnier, B., Tverberg, V., Gerland, S. . . . Dallmann, W. (2002). The physical environment of Kongsfjorden-Krossfjorden, an Arctic fjord system in Svalbard. *Polar Research*, *21*(1), 133–166.

Svendsen, H., & Thompson, R. (1978). Wind-driven circulation in a fjord. *Journal of Physical Oceanography*, *8*, 1–10.

Wang, D.-P., & Elliott, A. J. (1978). Non-tidal variability in the Chesapeake Bay and Potmac River: Evidence for non-local forcing. *Journal of Physical Oceanography*, *8*, 225–232.

Xu, Y., Rignot, E., Menemenlis, D., & Koppes, M. (2012). Numerical experiments on subaqueous melting of Greenland tidewater glaciers in response to ocean warming and enhanced subglacial discharge. *Annals of Glaciology*, *53*(60), 229–234.